Title

Recovering fetal signals transabdominally through interferometric near-infrared spectroscopy (iNIRS).

Journal

Biomedical Optics Express, 14(11)

ISSN

2156-7085

Authors

Liu, Shing-Jiuan

Lee, Su Yeon

Pivetti, Christopher

et al.

Publication Date

2023-11-01

DOI

10.1364/boe.500898

Peer reviewed

Research Article Vol. 14, No. 11 / 1 Nov 2023 / Biomedical Optics Express 6031
Biomedical Optics EXPRESS

Recovering fetal signals transabdominally through interferometric near-infrared spectroscopy (iNIRS)

SHING-JIUAN LIU,[1] SU YEON LEE,[2] CHRISTOPHER PIVETTI,[2] EDWIN KULUBYA,[2] AIJUN WANG,[2,3] DIANA L. FARMER,[2] SOHEIL GHIASI,[1] AND WEIJIAN YANG[1,*]

[1]Department of Electrical and Computer Engineering, University of California, Davis, Davis, CA 95616, USA
[2]Department of Surgery, University of California, Davis, Sacramento, CA 95817, USA
[3]Department of Biomedical Engineering, University of California, Davis, Davis, CA 95616, USA
[*]wejyang@ucdavis.edu

Abstract: Noninvasive transabdominal fetal pulse oximetry can provide clinicians critical assessment of fetal health and potentially contribute to improved management of childbirth. Conventional pulse oximetry through continuous wave (CW) light has challenges measuring the signals from deep tissue and separating the weak fetal signal from the strong maternal signal. Here, we propose a new approach for transabdominal fetal pulse oximetry through interferometric near-infrared spectroscopy (iNIRS). This approach provides pathlengths of photons traversing the tissue, which facilitates the extraction of fetal signals by rejecting the very strong maternal signal from superficial layers. We use a multimode fiber combined with a mode-field converter at the detection arm to boost the signal of iNIRS. Together, we can detect signals from deep tissue (>~1.6 cm in sheep abdomen and in human forearm) at merely 1.1 cm distance from the source. Using a pregnant sheep model, we experimentally measured and extracted the fetal heartbeat signals originating from deep tissue. This validated a key step towards transabdominal fetal pulse oximetry through iNIRS and set a foundation for further development of this method to measure the fetal oxygen saturation.

1. Introduction

The outcomes and costs associated with childbirth constitute a significant concern for both families and society as a whole. Compared to vaginal delivery, Cesarean section (C-section) has a higher cost, may increase the health risk to both the baby and mother, such as chronic lung conditions, post-operative infections, and massive hemorrhages [1,2], and has higher risks of complications in a subsequent pregnancy for the mother. Even though C-section may cause both financial and health problems, about 31.8% of the deliveries are via C-section [3], which is higher than the 10-15% ideal rate published by the World Health Organization [4,5]. A major factor for C-section delivery is the conservative prediction of fetal hypoxia during labor, which unfortunately has a high false-positive rate (60%) using the existing, widely-adopted electronic fetal monitoring technique through cardiotocography [6]. Efficacy-based studies show that cardiotocography increases the C-section rate but does not reduce fetal morbidity rates [4,7,8]. Transvaginal fetal pulse oximetry permits direct assessment of the fetal oxygen status and provides a better indicator of fetal well-being [9]. However, these benefits have not been realized due to concerns related to the risk of infection, interference with the natural progress of labor, or the possibility of the device slipping off the cheek of the fetus [10,11].

Transabdominal fetal pulse oximetry based on continuous-wave near-infrared spectroscopy (CW-NIRS) [12–14] has been proposed as a noninvasive approach to assess fetal oxygen saturation

#500898 https://doi.org/10.1364/BOE.500898
Journal © 2023 Received 18 Jul 2023; revised 30 Sep 2023; accepted 13 Oct 2023; published 31 Oct 2023

Biomedical Optics EXPRESS

[15–19]. It shines CW near-infrared light onto the maternal abdomen and detects the reflection at some distance away from the source point. Oxygen saturation level can be calculated by extracting the light absorption, which is modulated by the amount of heartbeat regulated oxygenated and deoxygenated hemoglobin in the tissues that the light traverses [20]. At least two detectors are placed apart to measure the light reflection. Detectors closer to the source point report the maternal signal, as the detected light mainly traverses the superficial maternal layer. Detectors farther from the source contain both weak maternal and fetal signals, as the detected light traverses deeper layers which also contain fetal tissue. The fetal signal can then be extracted through computational algorithms. The major challenge of this method is the low sensitivity of detecting fetal signals. It generally requires high light power which could raise safety concerns [19], or detectors with high sensitivity of light (such as photomultiplier tube) which could complicate the operation as it requires extensive dark environment. This challenge stems from the fact that fetus is located underneath thick tissue layers. The reflected light contains very few photons from the fetal layer.

In addition to CW-NIRS, frequency-domain (FD) NIRS [21–23], as a diffuse optical tomography method, has also been demonstrated to assess oxygen saturation in deep tissue such as fetus [24] or placentas [25] transabdominally. Though it also generally suffers from low sensitivity of deep tissue signals and requires measurement of multiple pairs of source-detector, FD-NIRS could measure additional tissue properties such as scattering coefficients through the multi-layer diffusion model. These facilitate the extraction of oxygen saturation. However, it generally requires the known tissue layer depth or initial guess of optical properties of the subject of interest (e.g. adipose, uterus, fetus) to fit the diffusion model, which complicates the overall measurement process. The fitting process generally requires intense computational resources [25]. Additionally, the tissue model needs to be updated when the fetus changes positions, which further increases the computational complexity.

Here, we propose a new method of transabdominal fetal signal extraction through interferometric near-infrared spectroscopy (iNIRS) [26–31] (Fig. 1). It is a time-domain interferometric technique that can provide a time-resolved reflectance or a time-of-flight (TOF) curve, which effectively separates signals originating from different tissue depths [26–31]. This allows us to use a single source and detector pair with a very short distance in between (so the overall photon collection efficiency is high) to detect the fetal signal without relying on the tissue model [32], representing a major advantage compared to CW-NIRS and diffuse optical tomography methods such as FD-NIRS. Furthermore, we innovatively employ a large core mode-field conversion fiber at the detection arm. This boosts the collection efficiency of the reflected light and increases the tissue depth that we can collect signals from. Such measures greatly increase the detection efficiency of fetal signal in deep tissue and reduce the required light power.

Using the proposed iNIRS approach, we experimentally measured the fetal heartbeat signal through the abdomen of pregnant sheep. This not only validated the key step in our long-term goal of transabdominal fetal pulse oximetry, but also demonstrated the high sensitivity of our method to detect fetal signals deep in the abdomen ($>\sim$1.6 cm, representing a large depth in reflection NIRS, with a source-detector separation at 1.1 cm), and separate it from the much stronger superficial maternal signal. Compared to CW-NIRS where the accessible depth is approximately a third to half of the source-detector separation [12,33], our detection depth is much larger. To the best of our knowledge, this is the first application of time-domain near-infrared spectroscopy in a two-subject model to extract individual signals. Our results pave a promising path towards transabdominal fetal pulse oximetry.

Biomedical Optics EXPRESS

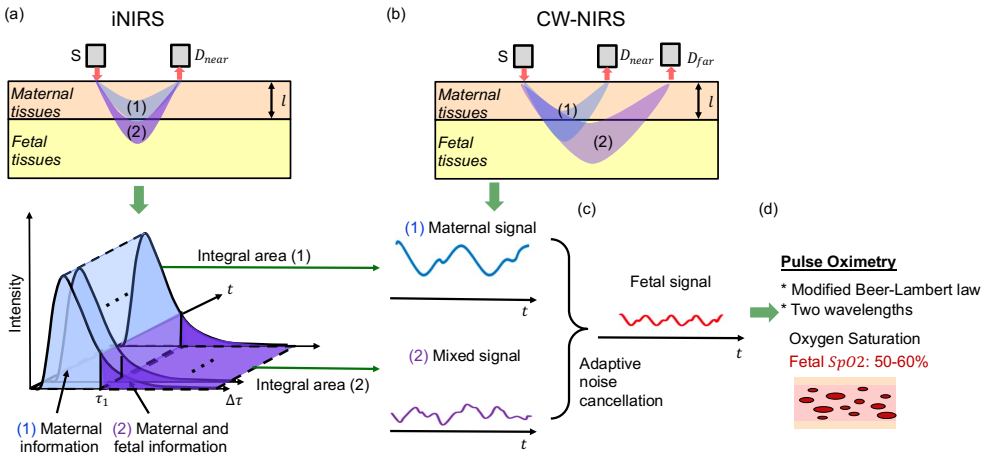

Fig. 1. An overview of transabdominal fetal pulse oximetry using iNIRS and CW-NIRS, and the associated fetal signal extraction process. (a) iNIRS. The frequency modulated light is sent into the sample and collected by a detector (D_{near}) close to the source. The collected signal from the sample interferes with a reference signal and provides a time-resolved reflectance, or time-of-flight (TOF) curve. (b) CW-NIRS. CW light is sent to the sample. In addition to D_{near}, a second detector (D_{far}) further away from the source is also needed. (c) Extraction of the fetal signal through adaptive noise cancellation. In iNIRS case, though there is only one detector (D_{near}) whose signal is dominated by the photons traversing superficial maternal tissue, the TOF curve is able to separate the early photons traversing only the superficial layers which carry the pure maternal signal [labeled as (1)], from the late photons traversing deep layers which carry mixed signals from both maternal and fetal tissue [labeled as (2)]. Pure fetal signal could then be extracted. In the CW case, the signal from D_{near} is approximated to be pure maternal [labeled as (1)], and that from D_{far} is the mixed signal [labeled as (2)]. (d) Calculation of fetal oxygen saturation SpO_2. From the modified Beer-Lambert law [34], light intensity fluctuation during a cardiac cycle could be converted to the alterations of the optical absorption and thus the volume of oxygenated and deoxygenated hemoglobin in the arteries. By measuring the light intensity signal in two wavelengths and leveraging the wavelength dependence absorption coefficient of oxygenated and deoxygenated hemoglobin, oxygen saturation can be derived (Supplement 1 Sec. 6).

2. Methods

2.1. *Monte Carlo simulation of near-infrared spectroscopy in a maternal-fetal two-subject reflection model*

We constructed a 3D pregnant human model composed of maternal and fetal tissue layers and used the Monte Carlo method to simulate light propagation in the tissue. Such simulations allow us to compare iNIRS and CW-NIRS for the transabdominal fetal pulse oximetry application, and study how the maternal, fetal, and mixed signal are impacted by the source-detector (SD) distance.

The 3D model of the abdomen of pregnant human is consisted of four tissue layers: the maternal abdominal wall, the uterus, the amniotic fluid, and the fetus. Each layer had a semi-spherical geometry and was characterized by its thickness and optical properties [18] (Table 1). We constructed three models with different fetal depths (1.8 cm, 2.9 cm and 4 cm) to cover a wide range of conditions in clinics [35] (Supplement 1). The fetal depth is measured as the minimum distance between the fetus and maternal skin. We used a GPU-based Monte Carlo eXtreme (MCX) package [36] to numerically analyze the photon propagation in the tissue. We launched

Biomedical Optics EXPRESS

720 million photons (N_{in}) at the wavelength of 850 nm from a small region on the maternal abdomen surface. Detectors were placed along the same abdomen surface with SD distance ranging from 0~6.4 cm. For the k^{th} photon received by the detector, we calculated its accumulated pathlength traversed in the maternal layer l_k^m and fetal layer l_k^f. We then counted the number of detected photons that traverse only the maternal layer (N_M) or both the maternal and fetal layer (N_{M+F}).

Table 1. Optical properties of tissue model [18,37–39][a]

Tissue Type	$\mu_a(mm^{-1})$	$\mu_s(mm^{-1})$	g	n	z_l (cm)
(1) Maternal abdominal wall	0.009	12.003	0.9	1.4	1.65
(2) Maternal uterus	0.01	8.15	0.9	1.4	1.15
(3) Amniotic fluid	0.004	0.1	0.9	1.334	0.1
(4) Fetal tissue	0.013	9.916	0.9	1.4	5.85

[a]μ_a, absorption coefficient; μ_s, scattering coefficient; g, anisotropy; n, refractive index at optical wavelength of 850 nm; z_l, layer thickness.

In Monte Carlo stimulation, there is no absorption event in the tissue. The true number of photons that are detected should take the absorption coefficient and the pathlength into account. We defined M_1 and M_2 as the true percentage of total detected photons and photons that traverse the fetal layer respectively, among the number of input photons:

$$M_1 = \left[\sum_{k\in\{N_M\}} \exp(-\mu_a^m l_k^m) + \sum_{k\in\{N_{M+F}\}} \exp(-\mu_a^m l_k^m - \mu_a^f l_k^f)\right] / N_{in} \tag{1}$$

$$M_2 = \left[\sum_{k\in\{N_{M+F}\}} \exp(-\mu_a^m l_k^m - \mu_a^f l_k^f)\right] / N_{in} \tag{2}$$

As the photons traverse in the maternal or fetal layer, their intensity is modulated by the amount of the change of oxygenated and deoxygenated hemoglobin during the cardiac cycle of the mother or fetus, which are integral components of the oxygen saturation calculation. Based on the modified Beer-Lambert law [34], the more the light travels through a particular layer (maternal or fetal), the more the light is affected by the cardiac cycle in that layer, and the better we may measure the oxygen saturation level in that layer. Thus, the strength of maternal signal (M_3) or fetal signal (M_4) is related to the total propagation pathlength of all detected photons in the corresponding layers.

$$M_3 = \sum_{k\in\{N_M\}} l_k^m \cdot \exp(-\mu_a^m l_k^m) + \sum_{k\in\{N_{M+F}\}} l_k^m \cdot \exp(-\mu_a^m l_k^m - \mu_a^f l_k^f) = M_{3,k\in\{N_M\}} + M_{3,k\in\{N_{M+F}\}} \tag{3}$$

$$M_4 = \sum_{k\in\{N_{M+F}\}} l_k^f \cdot \exp(-\mu_a^m l_k^m - \mu_a^f l_k^f) \tag{4}$$

$M_{3,k\in\{N_M\}}$ and $M_{3,k\in\{N_{M+F}\}}$ accounts for the photons propagating in the maternal layer only, and in both maternal and fetal layers respectively.

To analyze the pure fetal signal strength as compared to the overall detected signal (i.e. fetal signal contrast), we defined M_5 as the ratio between the summed photon pathlengths in fetal layer and the total photon pathlengths of all detected photons to represent the fetal signal contrast in CW-NIRS:

$$M_5 = \frac{M_4}{M_3 + M_4} \tag{5}$$

and M_6 as the ratio between the summed pathlengths in the fetal layers versus that in both fetal and maternal layers for the detected photons traversing the fetal layer for fetal signal contrast in

Biomedical Optics EXPRESS

iNIRS:

$$M_6 = \frac{M_4}{M_{3,k\in\{N_{M+F}\}} + M_4} \tag{6}$$

The analyze of matrices M_1~M_6 with respect to SD distance are shown in Section 3.1.

2.2. iNIRS setup with a compound collection fiber

iNIRS measures the time-resolved or pathlength-resolved near-infrared light reflecting from the tissue through an optical interferometer using a wavelength-swept laser source [26–31]. We implemented such a system on a portable, fiber-optics-based platform (Fig. 2(a), Supplement 1, Sec. 2 and 3). The laser light splits into two paths: the first path is the reference arm which consists of a single-mode fiber with known distance, and the second path is the sample arm where light gets reflected at different tissue depths and is then collected by a fiber. Light from the two paths then interferes with each other and generates a time-domain interference fringe pattern $I_{AC}(t)$, which could be expressed as $I_{AC}(\nu)$ with ν being the instantaneous frequency of the wavelength-swept laser. We calibrate optical frequency $\nu_0 + \Delta\nu(t)$ in the nonlinear sweep of the laser source through a known distance mismatch between the reference arm and sample arm in a calibration process [26,28,29]. The Fourier transformation of $I_{AC}(\nu)$ yields the time-resolved reflectance $I_{AC}(\tau)$, where τ is the delay time of the various pathlengths in the sample with respect to the reference arm (Supplement 1, Sec. 3). The TOF curve (Fig. 2(c)) effectively captures the optical pathlengths of light passing through both mother and fetus. The early and late segment of the TOF curve contains the pure maternal signal $I_{AC,\,superficial}$ and mixed signals $I_{AC,\,deep}$ from both maternal and fetal tissue (Supplement 1, Sec. 4). Adaptive noise cancellation [40] is then used to extract the fetal signal ($I_{AC,deep,fetal}$) by filtering out the maternal noise from the mixed signal (Supplement 1, Sec. 5). Finally, if the above procedure could be performed using two lasers with different central wavelengths, blood oxygen saturation can be analyzed for both mother and fetus (Supplement 1, Sec. 6).

In the experiment reported in this paper, our major goal is to validate if iNIRS can collect the photons traversing in the fetal layer in the deep tissue and recover $I_{AC,\,deep,\,fetal}$. Our experiment setup thus only contains a single laser (851 nm wavelength, 100 Hz wavelength sweeping rate). A collimated beam with a spot size of 4 mm and 50 mW is delivered to the tissue (an intensity below the American National Standards Institute maximum permissible exposure of 4 mW/mm^2). A detailed description of the experimental setup is presented in Supplement 1, Sec. 2.

Conventional iNIRS collects signal through a single mode fiber (SMF). The SMF for 851 nm has 4 µm/125 µm core/cladding diameter, with 0.13 NA. Such a small core and NA results in a very low efficiency to collect the diffusively reflective photons from the tissue. Here, we innovatively use a custom-made collection fiber to increase the collection efficiency. The collection fiber is composed of a short multimode fiber (MMF, 105 µm/125 µm core/cladding diameter, 0.22 NA), followed by a mode-field adaptor (MFA), and then the SMF. We term this fiber as compound fiber (Supplement 1, Sec. 7). The MFA is fabricated by thermally expanding the core of SMF and then splicing to the MMF [41,42]. Compared to a regular SMF fiber, the compound collection fiber has a wider distal end and a higher NA (MMF section), and could thus collect more light. It could collect higher order modes, which could subsequently convert to the fundamental mode of the SMF through the MFA (with a mode-dependent conversion efficiency). This ensures the signal integrity for the interference with light from the reference arm which is an SMF.

2.3. Numerical simulation of fiber collection efficiency in iNIRS

As the mode conversion from MMF to SMF encounters substantial loss, we investigated if the compound collection fiber has an effectively higher light collection efficiency than an SMF in iNIRS. Using a Finite Difference Beam Propagation Method (FD-BPM) [43], we conducted numerical simulations of light propagation through the SMF and compound fiber. In these

Biomedical Optics EXPRESS

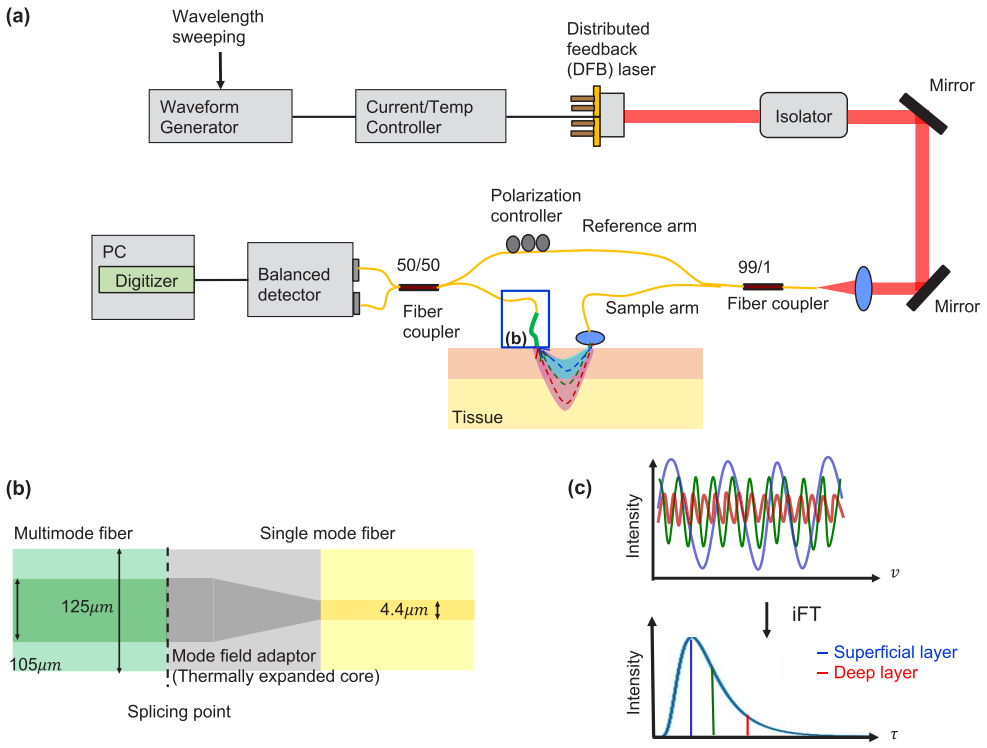

Fig. 2. (a) Schematics of the fiber-based iNIRS setup. (b) Collection fiber of the sample arm, which is composed of a short segment of multimode fiber, mode field adaptor (thermally expanded core fiber) and single mode fiber. (c) Illustration of the time-domain interference signals between light from the reference arm and sample arm with three different pathlengths (top), and the corresponding signal in the time-of-flight curve (bottom). A smaller/longer pathlength (delay) indicates light reflected at the superficial/deep tissue layer and thus has a larger/small intensity (blue/red).

simulations, we utilized speckle patterns, which represent the scattered light field at the tissue surface, as the input light field for both the SMF and compound fiber configurations. To generate these speckle patterns, we first found all the eigenmodes (5000) of a fiber with a high Numerical Aperture (NA). We assigned complex coefficients, consisting of both real and imaginary components, to each mode. These coefficients were independently and identically distributed, following a 2D Gaussian distribution, as detailed in Supplement 1, Sec. 7. We then summed up the complex field of all 5000 eigenmodes, which resulted in the speckle patterns. We note the NA set in the fiber where we extracted the eigenmodes was larger than that of the SMF and MMF. This ensures that the speckle patterns are fully developed from the perspective of the SMF and MMF, matching the experimental conditions of diffusion regime, where our interest is to collect the late arrival photons with long pathlength. The simulation results are presented in Section 3.2.

2.4. *Experimental characterization of fiber collection efficiency in iNIRS in one subject transmission model*

We validated our experimental setup in phantom samples and compared the TOF reflectance intensity using the regular SMF collection fiber and the custom-made compound collection fiber. The phantom samples were whole milk mixed with water in glass petri dishes, with five different

Biomedical Optics EXPRESS

concentrations of milk ($\boldsymbol{c}$ = 12.5%, 15%, 20%, 25%, 30%). These fluid phantoms were placed in the sample arm, respectively, in the transmission geometry of iNIRS (Supplement 1, Sec. 8).

We fit the experimentally measured TOF data to the diffusion theory so as to derive the phantom's optical properties (Supplement 1, Sec. 9). We carefully selected the fitting region, commencing from a 100 ps delay from the peak of the TOF curve. This selection ensured the validity of the diffusion approximation for radiative transport.

To quantify the advantage of using a compound fiber over an SMF in terms of light collection in the fully diffused conditions, we summed up the intensities of the TOF curve within the fitting region. This sum is denoted as $P_{diffuse}^{compound}$ for the compound fiber and $P_{diffuse}^{SMF}$ for the SMF fiber. The ratio of $P_{diffuse}^{compound}$ to $P_{diffuse}^{SMF}$ under different milk concentrations are summarized and analyzed in Section 3.3.

2.5. Measurement of the light penetration depth on highly scattered tissue in one-subject reflection model

We next examined the robustness of iNIRS against the light penetration depth in the highly scattered tissue. As a baseline, we evaluated the signal quality from superficial tissue by placing the source and detector on a human forearm (1.1 cm SD distance) and measuring the heartbeat signal from the radial arterial vascular tissue in the reflection geometry. The radial artery is estimated to be 4.5 - 5.8 mm depth for female subjects [44]. We performed measurements over 2 minutes at a temporal resolution of 5 ms. To evaluate the signal quality from deeper tissue, we placed thin pork slices (~1.5 mm thick per slice) on the same measurement location in the forearm, and then placed the source and detector on top of the pork slices. We used the Signal-to-Noise Ratio (SNR) to quantify the heartbeat signal. The SNR is defined as the ratio between the peak amplitude of the heartbeat signal and the standard deviation of the noise floor in the Fourier spectrum. These SNR measurements are detailed and summarized in Section 3.4, which provides insights into the performance of iNIRS in different tissue depths and scattering conditions.

2.6. Measurement of the fetal heart rate in pregnant sheep in two-subject reflection model

We evaluated if the iNIRS could measure and recover the fetal signal $I_{AC,deep,fetal}(t)$ and its heartbeat in a pregnant sheep model. The procedures (Supplement 1, Sec. 10) used were approved by the UC Davis Institutional Animal Care and Use Committee. Briefly, the fetus was exposed by vertical laparotomy and hysterotomy to allow for fetal carotid artery cannula insertion to obtain fetal heartbeat through hemodynamic monitoring as the ground truth. Those incisions were then closed and deterministic tissue geometry of the abdomen and uterus in the pregnant sheep was obtained. The baseline of the maternal heartbeat was monitored by a conventional pulse oximeter placed on the abdomen. To perform the iNIRS measurement, we put the source and detector 1.1 cm apart on top of the pregnant sheep abdomen in a region where the distance of the source and detector to the fetus was estimated to be minimum. The experiments were performed on a total of 3 sheep. The three fetal lambs were 8~11 mm below the maternal abdomen and the uterus wall was 5~9 mm thick, resulting in 16~17 mm fetal depth in total (Table 2). For each sheep experiment, we obtained the TOF curves over 1 minute of measurement time at a temporal resolution of 5 ms. The heartbeat measurement from iNIRS was then compared to the ground truth, obtained by the conventional pulse oximeter for the mother and the hemodynamic monitor for the fetus. The results are presented in Section 3.5.

Biomedical Optics EXPRESS

3. Results

3.1. iNIRS shows a higher fetal signal strength and contrast than CW-NIRS in the Monte Carlo simulation of a maternal-fetal two-subject reflection model

In the Monte Carlo simulation of the maternal-fetal two-subject reflection model (Fig. 3(a), with a fetal depth of 2.9 cm, which is the average fetal depth at gestation of 40 weeks [35]; see Supplement 1 Sec. 1 for fetal depth of 1.8 cm and 4 cm), as the SD distance increases, the normalized number of total detected photons M_1 and those that traverse the fetal layer M_2 decreased with the increase of the SD distance. The maternal signal strength M_3 and fetal signal strength M_4 show the same trend, even though the pathlength of each photon increases (Fig. 3(b)). M_2 approached M_1 as SD distance increases, indicating that an increasing portion of detected photons have propagated in the fetal layer.

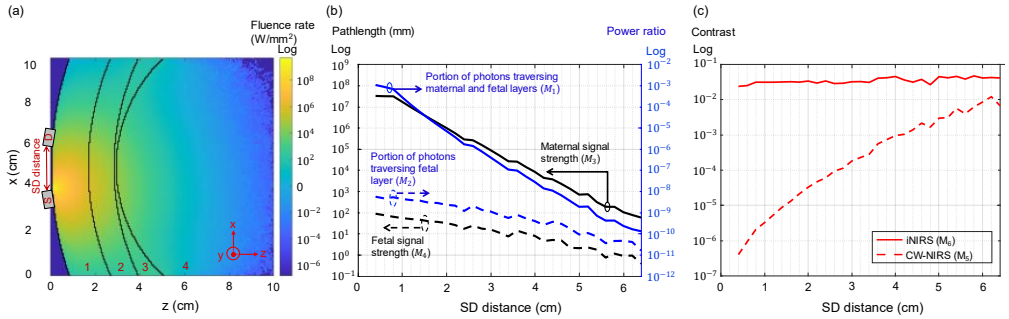

Fig. 3. (a) A cross-section view of the 3D tissue model used in the Monte Carlo simulations. The model was constructed based on the pregnant human which consisted of four spherical regions (Table 1), and was rotationally symmetry along axis $x = 5$ *cm*. The source (S) and detector (D) were positioned at the surface of layer 1, symmetrically along axis $x = 5$ *cm*. The fetal depth was 2.9 cm. (b) The evaluated metrics ($M_1 \sim M_4$) for SD distance ranging from 0~6.4 cm. (c) The fetal signal contrast of CW-NIRS (M_5) and iNIRS (M_6) for different SD distances.

In CW-NIRS transabdominal fetal pulse oximetry, each detector does not distinguish what tissue layers the photons traverse. To achieve a high detection sensitivity of fetal signal, it is desirable to have a large fetal signal strength M_4 and a small maternal signal strength M_3. The latter translates to a higher fetal signal contrast M_5. However, there is no proper detector configuration that can simultaneously achieve large M_4 and small M_3 (or larger M_5) (Fig. 3(b)). The detector with a small SD distance is dominated by signal of the superficial maternal layers and has a very low fetal signal contrast M_5 (Fig. 3(c)). Therefore, extracting the fetal signal from the deep tissue is challenging. Detectors with large SD distances contain a higher proportion of photons that reach the deep fetal layer (i.e. high fetal signal contrast M_5), but the detected signals are noisy and weak (low fetal signal strength M_4) due to the long photon pathlength. To reach a reasonable SNR at a large SD distance, it requires a very high input light power to the tissue, raising the bio-safety concerns.

iNIRS measures the TOF reflectance and can separate the signal with different photon pathlengths. The early arrival photons (mostly from superficial tissue) are present in the early TOF reflectance curve while the late arrival photons (from the deep tissue) are located at the tail of the TOF reflectance curve. We can choose a small SD distance when the fetal signal M_4 is strong (Fig. 3(b)). Even though the CW fetal signal contrast M_5 is small (Fig. 3(c)), we can reject the strong superficial layer signal and take out the deep layer signal from the TOF reflectance curve as long as the signal is above the noise floor. iNIRS thus achieves a higher fetal signal

Biomedical Optics EXPRESS

contrast (M_6) than CW-NIRS (M_5), particularly in short SD distance. In our experiment, we used a SD distance ~1.1 cm, where the source fiber coupler and detection fiber were placed side by side. With the ability to separate photons traversing superficial layers (capturing pure maternal signal) and deep layers (capturing the mixed maternal and fetal signal), a single detector in iNIRS can provide all the information that is captured by multiple detectors in CW-NIRS (detectors with small and large SD distance to capture the pure maternal signal and the mixed signal respectively). From this analysis, we concluded that iNIRS has a greatly increased sensitivity to deep tissue signal though only a single detector is used.

3.2. Compound fiber shows higher collection efficiency than single mode fiber in simulation

In the beam propagation simulation, we analyzed the light power that was collected by the pure SMF and compound fiber, for 20 independently generated speckle patterns as the input light field (Fig. 4(a)). As the light field propagated in the fiber, the power decreased and the light field gradually converged to the single mode of SMF (Fig. 4(b)-(c)). While the remaining power at the exit of the SMF for both the pure SMF and compound fiber varied for each speckle pattern, on average the remained light power in the compound fiber was 3.4× larger than that of the pure SMF (Fig. 4(d)-(e)). In our experiment, the speckle likely changed faster than one laser swept duration, so experimentally during one sweep we likely measured the average speckle patterns. This result indicates that the compound fiber could indeed benefit the detection of the photons scattered from deep tissue.

3.3. Compound fiber shows higher signal quality than single mode fiber in one subject transmission model

We performed the iNIRS measurements in the phantom of five different concentrations of whole milk in water (Fig. 5(a)-(b)) and obtained the TOF curves (Fig. 5(c)-(d), Supplement 1, Sec. 8). For both SMF and the compound fiber, the TOF distribution curves were broadened and attenuated with increasing milk concentration. This was expected as a higher milk concentration increased the light scattering and thus increased the overall light pathlength. Fitting the TOF curve with the diffusion theory indeed showed a higher reduced scattering coefficient as the milk concentration increased (Fig. 5(e)). Compared with the SMF case, the compound fiber resulted in a TOF curve with a higher intensity but similar distribution as the underlying sample was the same. Quantitatively, the summed intensity under the TOF curve at the diffusion regime for the compound fiber $P_{diffuse}^{compound}$ was ~4× than that of the SMF $P_{diffuse}^{SMF}$, averaged across the different milk concentrations. This is in a reasonable agreement with the numerical simulation in Section 3.2. Our result confirmed that the compound fiber can measure the TOF curve with a higher collection efficiency than SMF. To detect weak-intensity photons that traverse deep tissue (Section 3.4-3.5), such an enhanced throughput of the compound fiber is highly beneficial.

3.4. iNIRS detects heartbeat signal in highly scattered tissue in one-subject reflection model

We performed iNIRS measurements on the human forearm over a time course of 2 minutes (Fig. 6(a)). At each measurement time stamp, we extracted a TOF reflectance curve. We divided each TOF reflectance curve into two sections (Fig. 6(b)) to separate the early arrival photons (section 1) and late arrival photons (section 2). The summation of the area under the curve of section 1 and 2, respectively represents the signal of the photons propagating through the superficial layers only, and those down to the deeper layers and scattered back to the surface. In the time domain, such a signal is presumably modulated strongly by the blood volume in the artery and synchronized with the cardiac cycle. Indeed, the Fourier spectrum of the signal from either section 1 or 2 clearly revealed the heartbeat signal (1.34 Hz) and its harmonic term

Biomedical Optics EXPRESS

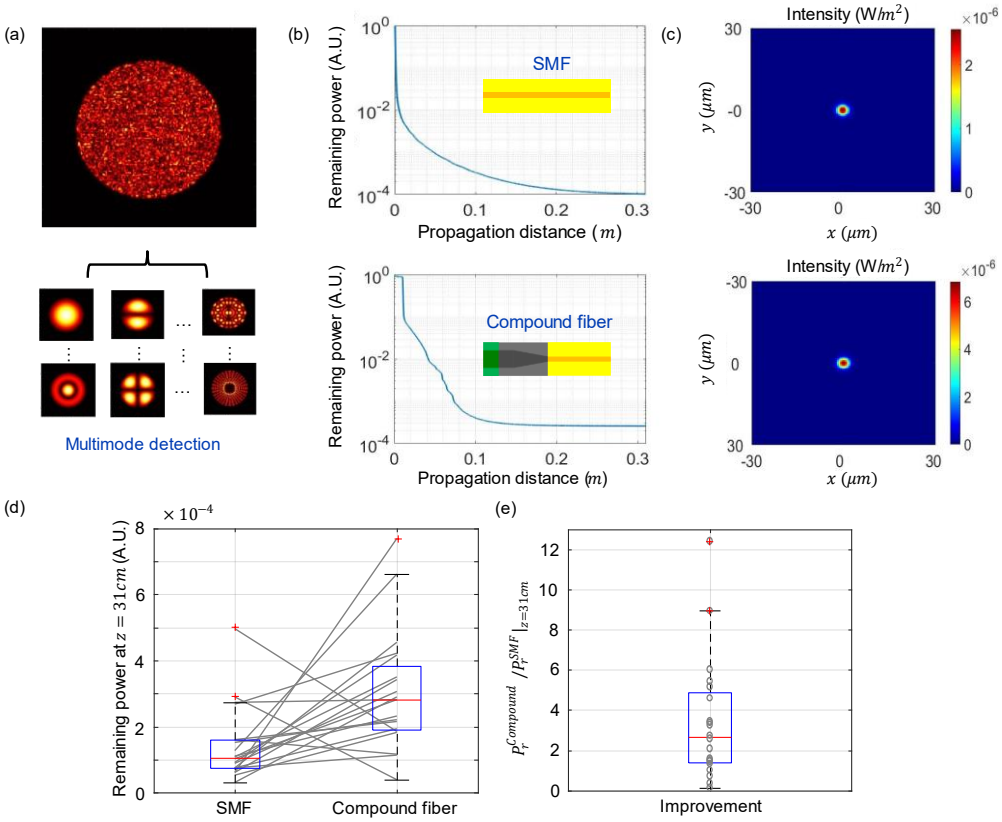

Fig. 4. (a)-(c) A representative speckle pattern and its mode decomposition. (a) The speckle patterns were used to represent the light field exiting the scattered tissue. They were formed by summing the modes of a high NA multimode fiber whose complex weights were independently sampled following a 2D Gaussian distribution. (b) The remaining power (normalized to the power of the speckle pattern) $P_{r,z}$ along the propagation distance z when light from the speckle patterns propagated along the SMF (top) and compound fiber (bottom). In this simulation, the compound fiber was composed of 1 cm MMF, 6 cm length MFA, and 24 cm SMF. (c) The spatial intensity at z = 31 cm for both SMF (top) and compound fiber (bottom). (d) The remaining power at the SMF and compound fiber at z = 31 cm, for 20 different speckle patterns (each synthesized from 5000 modes). (e) The ratio of the remaining power at compound fiber versus the SMF at z = 31 cm, for 20 different speckle patterns. The Boxplot summarizes the data statistically. Center bars (red), medians; box edges, first and third quartiles, respectively; whiskers, minimum and maximum; + mark, outliner. The 20 speckle patterns were formed by superimposing spatial modes with 20 different sets of complex mode coefficients drawn from the 2D Gaussian distribution. z = 31 cm was the exit of both SMF and compound fiber.

(2.68 Hz) (Fig. 6(c)). We also plotted the Fourier spectrum of the signal summed from both section 1 and 2 (Fig. 6(c)), which essentially mimics the CW-NIRS measurement. We again saw both the fundamental tone and harmonic term. This was not surprising as the artery under the measurement was located close to the tissue surface, so most of the collected photons traversed the artery, and thus both CW-NIRS and iNIRS worked well.

To evaluate the signal quality from deeper tissue, we placed thin pork slices (~1.5 mm thick per slice) on the same measurement location in the forearm, which effectively increases the depth

Biomedical Optics EXPRESS

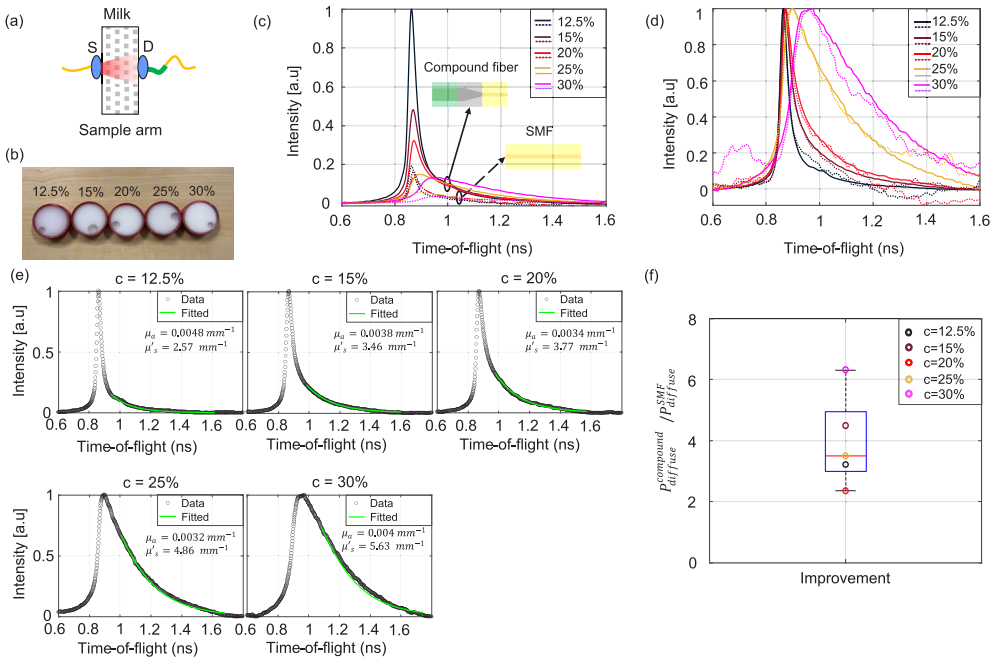

Fig. 5. (a) iNIRS measurement of milk samples in transmission mode. The source and detector, each connected to a lens with NA = 0.5 (which is larger than the NA of both SMF and MMF) were aligned to maximize the power of detected light before the fluid phantoms were inserted. (b) The fluid phantoms with various concentrations of whole milk (12.5%, 15%, 20%, 25%, 30%) in water. (c, d) The photon TOF distributions using SMF or compound fiber as the collection fiber for the various milk concentrations. (c) The TOF curves were nominalized to the peak value of 12.5% milk concentration using the compound fiber. (d) Each TOF curve was normalized to its own peak. (e) TOFs data (black dot), fitted curve to the radiative transfer equation (green line), and extracted optical properties for samples with different milk concentrations. The fitting region starts from a 100 ps delay from the peak of TOF curve, which ensured the validity of the diffusion approximation for radiative transport. (f) The improvement of the compound fiber as compared to SMF for five different milk concentrations, respectively. The Boxplot summarizes the data statistically. Center bars (red), medians; box edges, first and third quartiles, respectively; whiskers, minimum and maximum.

of the artery (Fig. 6(d)). Figure 6(e) shows the extracted TOF reflectance curve where seven pork slices (~10.5 mm thick in total) were added on top of the forearm, resulting in an effective artery depth of ~15-16.3 mm. We again separated the TOF curve into two sections. Contrary to the previous experiments without pork slices, the Fourier spectrum of the signals integrated from both sections did not show any heartbeat signal (Fig. 6(f)). This indicates that, as the artery was deep into the tissue, its signal was overwhelmed by the strong signals from the superficial tissues, and the CW-NIRS failed to extract the useful signal at this SD distance. In iNIRS, we could extract the photons traversing deep into the tissue (section 2), and the Fourier spectrum of the signal integrated from section 2 alone showed the heartbeat signal (1.15 Hz). We found that excluding the photons towards the tails of the TOF curve in section 2 (i.e. only accounting signals in section 3 at Fig. 6(e)) could further enhance the signal of the heartbeat, presumably because the particularly late photons had low overall intensity and they traversed deeper than the radial artery and carried weak pulsation signal.

Biomedical Optics EXPRESS

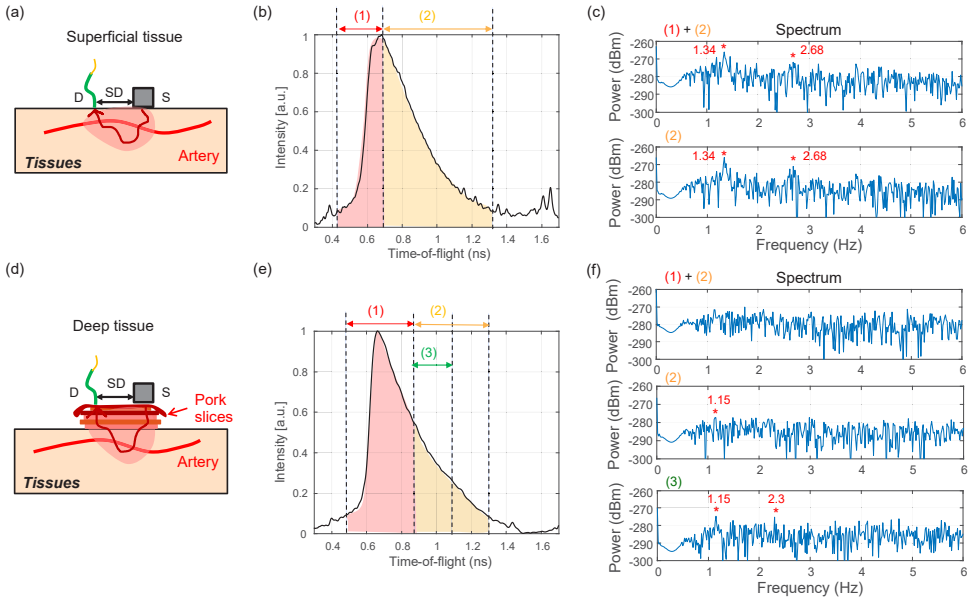

Fig. 6. iNIRS was performed noninvasively in the human forearm in vivo in reflection mode. (a) The source and detector were attached to the tissue surface. The source fiber was connected to a lens with NA = 0.5. No lens was connected to the detection fiber, which simplified the operation while keeping a high collection efficiency. (b) The measured TOF curve is separated in section (1) and (2) and the area below it is colored red and orange, respectively. (c) The Fourier spectrums of the selected TOF area in (b) versus measurement time. Peaks in the power spectra, indicated by asterisks, correspond to physiological changes / heartbeat in the tissue (or their harmonics). (d-f) Same as (a)-(c), but with seven pork slices inserted between the human forearm and the source and detector. By properly segmenting the TOF reflectance curve and analyzing the signals at section (3), a clear heartbeat signal could be obtained.

We further quantified the SNR of the heartbeat signal extracted from iNIRS measurements with different numbers of pork slices (Fig. 7). As the number of pork slices increased, the overall SNR dropped. Nonetheless, we achieved an SNR of ~7.77 dB for the condition of seven pork slices on top of the forearm (~15-16.3 mm effective artery depth). Overall, this set of experiment suggests that the deep tissue signal could be extracted under multiple tissue layers by properly segmenting the TOF reflectance curve.

3.5. iNIRS detects fetal heartbeat signal through maternal abdomen

We performed iNIRS measurements on a pregnant sheep model (Fig. 8(a)-(b)). We again segmented each measured TOF curve into two sections (Fig. 8(c)). The summation of signals in both sections represents the CW-NIRS measurement. The Fourier spectrum of this summation revealed the fundamental and harmonic tone of the maternal heartbeat signal, but not the fetal heartbeat signal (Fig. 8(d)). This is expected as only a small proportion of photons reaching the detector traversed the fetal tissues at such a small SD distance, and the total signal was dominated by the maternal signal. Extracting the photons in the early TOF curve (i.e. section 1) resulted in a stronger maternal signal strength (Fig. 8(e)), attributed to the higher maternal signal contrast obtained by the TOF curve. However, enclosing all the late photons in section 2 of the TOF curve revealed neither the maternal signal nor the fetal signal (Fig. 8(f)). By removing those photons at the tails of section 2 (thus only accounting signals in section 3 in Fig. 8(c)), we were able to

Biomedical Optics EXPRESS

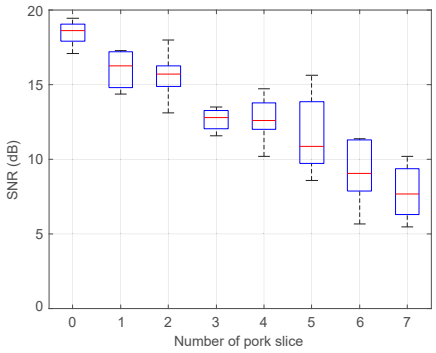

Fig. 7. SNR versus the number of pork slices to evaluate the tissue penetration depth of iNIRS measurements. Since the strength of the signal could be influenced by the precise anatomical characteristics of the artery, we conducted multiple measurements by positioning the source and detector at various locations on the forearm for a more robust assessment. Six measurements at different positions on the arm were conducted for each condition of the pork slice number. Each pork slice was ~1.5 mm in thickness and the overall penetration depth including 7 pork slices and radial artery depth was around 15-16.3 mm. The boxplot summarizes the data statistically. Center bars (red), medians; box edges, first and third quartiles, respectively; whiskers, minimum and maximum.

obtain both clear maternal heartbeat and clear fetal heartbeat signal (Fig. 8(g)). This indicates that the photons with particularly long pathlength may carry weak or noisy fetal and maternal signals, presumably related to the exact tissue geometry. We used the adaptive noise cancellation method to filter away the "maternal noise" from the mixed signal. The maternal signal from section (1) (Fig. 8(e)), and the mixed signal from section (3) (Fig. 8(g)) were considered as the noise and signal respectively. Assuming that the signal and noise were uncorrelated, the adaptive noise cancellation algorithm could remove the maternal signal from the mixed signal to obtain a clean fetal heartbeat signal (Fig. 8(h)).

Table 2. Comparison of the fetal and maternal sheep heart rate measured by iNIRS and the conventional pulse oximeter or hemodynamic monitor (ground truth), over a total of 10 minutes

	Thickness (mm)	iNIRS (Hz)		Ground truth (Hz)		Max error (Hz)	
Sheep	Abdomen/Uterus	Mother	Fetus	Mother	Fetus	Mother	Fetus
Sheep 1	8 / 9	1.36±0.01	3.21±0.17	1.39 ± 0.06	3.38±0.14	-0.08	-0.2
Sheep 2	11/ 5	1.52±0.02	2.27±0.3	1.51±0.04	2.13 ± 0.13	-0.03	0.31
Sheep 3	9/ 7	1.17±0.15	2.65±0.29	1.19±0.1	2.54 ± 0.22	0.03	0.18

We compared the extracted maternal heart rate and fetal heart rate using iNIRS with the ground truth obtained by the conventional pulse oximeters directly attached to the maternal tissue and the hemodynamic monitor from the fetal carotid artery line (Table 2). Excellent agreement was achieved between the iNIRS and the ground truth, with a maximum error of 0.047 Hz (3.4%) for maternal heart rate and 0.23 Hz (9.2%) for fetal heart rate over a total of 10 minutes recording, averaged across three sheep experiments. This demonstrated the robustness of our method.

Biomedical Optics EXPRESS

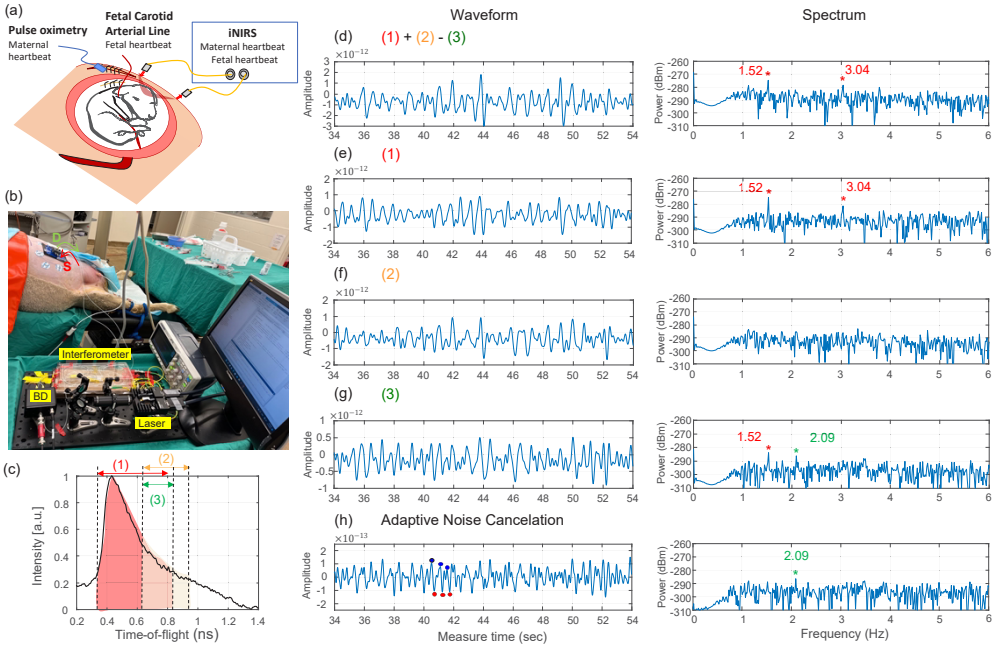

Fig. 8. Heartbeat measurement of fetus in a pregnant sheep model. (a) Illustration of the three probes of heartbeat measurement on a pregnant sheep: proposed iNIRS laid on the maternal abdomen to measure the maternal and fetal heartbeat; fetal carotid artery line cannulated into the fetal neck to obtain fetal heartbeat as the ground truth; conventional pulse oximetry clipped to the mother's abdomen to measure maternal heartbeat as the ground truth. (b) A photo of the iNIRS setup using an interferometer with a laser diode and balance detector (BD) during the fetal lamb heartbeat measurements. A pair of source (S in red) and detector (D in green) was placed on the maternal abdomen. (c) The TOF curve captured from the iNIRS with three different TOF segments. (d)-(g) present the temporal waveform (left) and frequency power spectra (right), extracted from different TOF segments in (c). (h) Signals after feeding (e) and (g) to the adaptive noise cancellation algorithm. In the power spectra, the asterisks indicate the heartbeat signal (or their harmonics) in the tissue. The red and green asterisks correspond to those for the mother and fetus respectively. In the temporal waveform panel of (h), the blue and red dots serve as examples to illustrate the diastolic and systolic cycle, corresponding respectively to the minima and maxima of light absorption of the hemoglobin. In this experiment, the thickness of the maternal abdomen and uterus was about 11 mm and 5 mm, respectively.

4. Discussion

We demonstrated the application of iNIRS in transabdominal fetal pulse oximetry to recover fetal signal. We innovatively used a multimode fiber and mode-field adaptor to increase the collection efficiency of the scattered photons from the tissue and thus extend the tissue depth that it could collect signal from. We experimentally demonstrated that the fetal heart rate could be extracted by placing a compact size optical probe on the abdomen of pregnant sheep, from fetus located $>\sim$1.6 cm depth in mother's uterus with a small SD distance and low optical power. Our method highlights the great promise of extracting the fetal oxygen saturation by incorporating a second laser at a different wavelength in an iNIRS setup, as a future work.

Compared to other existing NIRS methods of measuring the biological properties of deep scattering tissue such as those in CW [15–18] or frequency-domain [24,25], iNIRS stands out as

Biomedical Optics EXPRESS

it provides depth information, leading to a high detection sensitivity of deep tissue signal, low light power, and use of a single probe setup on tissue surface. As a general approximation, the penetration depth achievable is approximately a third to half of the SD separation distance in NIRS [12,33]. At greater SD separation distances, deeper penetration of light is achieved at the cost of poorly resolved signal due to less light being captured by the detector. This in return requires high light power, raising safety concerns. Furthermore, at least two detectors at different SD distances are needed to separate the maternal and fetal signal. This is in sharp contrast with iNIRS, where different photon pathlengths could be readily obtained from a single SD distance, and we could reliably detect signals at 1.6 cm depth with a 1.1 cm SD distance.

Conventional TD-NIRS [45] could resolve TOF information by delivering a train of picosecond laser pulses to the tissue and analyzing the reflected signal as a function of time. However, most of the modern TD-NIRS instruments utilize expensive pulsed lasers and complex time-correlated single photon counting detection [46,47], making the widespread adoption of this technology challenging. In comparison, iNIRS is much more cost-effective.

While iNIRS enables deep tissue measurements at short SD separation, the depth penetration, and thus the signal at the tails of the TOF curve, remains limited by the throughput of the collection fiber. This problem can be addressed partially using the expanded fiber core to collect more diffused and reflected photons on the tissue surface. We used a compound fiber which contains MMF, MFA, and SMF [41,42]. The MMF has a high optical throughput, and MFA converts the MMF modes into the fundamental mode of SMF for heterodyne interferometry. Compared to a pure SMF, the compound fiber achieves ~3×-4× increase of signal, facilitating the detection of the weak signal from deep scattering tissue. To translate this work to human pregnancy models, which have a larger fetal depth compared to the pregnant sheep model used here, further increase of the collected signal is likely necessary. This remains an important problem to solve in the future.

Finally, the current system includes only one wavelength source, which does not allow the extraction of oxygenation saturation level. Our future work includes extending this technique to multiple sources by wavelength division multiplexing, and to derive the relative concentration of oxygenated (HbO2) and deoxygenated (Hb) hemoglobin thereby calculating the oxygenation saturation level.

Funding. Burroughs Wellcome Fund (1015761); National Institute of Biomedical Imaging and Bioengineering (P41EB032840); National Science Foundation (1838939).

Acknowledgement. We thank Dr. Vivek Jay Srinivasan, Dr. Wenjun Zhou and Dr. Dibbyan Mazumder for fruitful discussion on iNIRS.

Disclosures. W. Yang, S.-J. Liu and S. Ghiasi are listed as inventors of the patent application: "Transabdominal fetal oximetry based on frequency-modulated continuous-wave near-infrared spectroscopy" (2021, PCT/US2021/060875).

Data availability. Data underlying the results presented in this paper are not publicly available at this time but may be obtained from the authors upon reasonable request.

Supplemental document. See Supplement 1 for supporting content.

References

1. C. R. Cardwell, L. C. Stene, G. Joner, O. Cinek, J. Svensson, M. J. Goldacre, R. C. Parslow, P. Pozzilli, G. Brigis, D. Stoyanov, B. Urbonaitė, S. Šipetić, E. Schober, C. Ionescu-Tirgoviste, G. Devoti, C. E. de Beaufort, K. Buschard, and C. C. Patterson, "Caesarean section is associated with an increased risk of childhood-onset type 1 diabetes mellitus: a meta-analysis of observational studies," Diabetologia **51**(5), 726–735 (2008).
2. A. K. Hansen, K. Wisborg, N. Uldbjerg, and T. B. Henriksen, "Risk of respiratory morbidity in term infants delivered by elective caesarean section: cohort study," BMJ **336**(7635), 85–87 (2008).
3. M. Osterman, B. Hamilton, J. Martin, A. Driscoll, and C. Valenzuela, "Births: Final Data for 2020.," presented at the Natl Vital Stat Rep.2021.
4. "Appropriate technology for birth," *Lancet* 2, 436–437 (1985).
5. "WHO Statement on caesarean section rates World Health Organization Human Reproduction Programme, 10 April 2015," Reprod Health Matter **23**(45), 149–150 (2015).

Biomedical Optics EXPRESS

6. A. Pinas and E. Chandraharan, "Continuous cardiotocography during labour: Analysis, classification and management," Best Pract Res Clin Obstet Gynaecol **30**, 33–47 (2016).
7. K. B. Nelson, T. P. Sartwelle, and D. J. Rouse, "Electronic fetal monitoring, cerebral palsy, and caesarean section: assumptions versus evidence," BMJ **355**, i6405 (2016).
8. Z. Alfirevic, D. Devane, G. M. L. Gyte, and A. Cuthbert, "Continuous cardiotocography (CTG) as a form of electronic fetal monitoring (EFM) for fetal assessment during labour," Cochrane Database of Systematic Reviews (2017).
9. E. Ce, C. Pb, B. Lm, and B. Sp, "Update on intrapartum fetal pulse oximetry," Aust. N. Z. J. Obstet. Gynaecol. **42**, 119–124 (2002).
10. C. E. East, L. Begg, P. B. Colditz, and R. Lau, "Fetal pulse oximetry for fetal assessment in labour," Cochrane Database Syst Rev **2014**, 1 (2014).
11. T. Uchida, N. Kanayama, K. Kawai, M. Mukai, K. Suzuki, H. Itoh, and M. Niwayama, "Reevaluation of intrapartum fetal monitoring using fetal oximetry: A review," J Obstet Gynaecol Res **44**(12), 2127–2134 (2018).
12. G. Strangman, D. A. Boas, and J. P. Sutton, "Non-invasive neuroimaging using near-infrared light," Biol. Psychiatry **52**(7), 679–693 (2002).
13. M. Ferrari and V. Quaresima, "A brief review on the history of human functional near-infrared spectroscopy (fNIRS) development and fields of application," NeuroImage **63**(2), 921–935 (2012).
14. F. Scholkmann, S. Kleiser, A. J. Metz, R. Zimmermann, J. M. Pavia, U. Wolf, and M. Wolf, "A review on continuous wave functional near-infrared spectroscopy and imaging instrumentation and methodology," NeuroImage **85**, 6–27 (2014).
15. A. Zourabian, A. Siegel, B. Chance, N. Ramanujan, M. Rode, and D. A. Boas, "Trans-abdominal monitoring of fetal arterial blood oxygenation using pulse oximetry," J. Biomed. Opt. **5**(4), 391–405 (2000).
16. A. M. Vintzileos, S. Nioka, M. Lake, P. Li, Q. Luo, and B. Chance, "Transabdominal fetal pulse oximetry with near-infrared spectroscopy," Am. J. Obstet. Gynecol. **192**(1), 129–133 (2005).
17. D. D. Fong, A. Knoesen, M. Motamedi, T. O'Neill, and S. Ghiasi, "Recovering the fetal signal in transabdominal fetal pulse oximetry," Smart Health **9-10**, 23–36 (2018).
18. D. D. Fong, K. Vali, and S. Ghiasi, "Contextually-aware Fetal Sensing in Transabdominal Fetal Pulse Oximetry," Acm Ieee Int Conf Cy **1**, 119–128 (2020).
19. D. D. Fong, K. J. Yamashiro, K. Vali, L. A. Galganski, J. Thies, R. Moeinzadeh, C. Pivetti, A. Knoesen, V. J. Srinivasan, H. L. Hedriana, D. L. Farmer, M. A. Johnson, and S. Ghiasi, "Design and In Vivo Evaluation of a Non-Invasive Transabdominal Fetal Pulse Oximeter," IEEE Trans. Biomed. Eng. **68**(1), 256–266 (2021).
20. P. D. Mannheimer, J. R. Casciani, M. E. Fein, and S. L. Nierlich, "Wavelength selection for low-saturation pulse oximetry," IEEE Trans. Biomed. Eng. **44**(3), 148–158 (1997).
21. B. Chance, M. Cope, E. Gratton, N. Ramanujam, and B. Tromberg, "Phase measurement of light absorption and scatter in human tissue," Rev Sci Instrum **69**(10), 3457–3481 (1998).
22. T. D. O'Sullivan, A. E. Cerussi, D. J. Cuccia, and B. J. Tromberg, "Diffuse optical imaging using spatially and temporally modulated light," J. Biomed. Opt. **17**(1), 0713111 (2012).
23. S. Fantini and A. Sassaroli, "Frequency-Domain Techniques for Cerebral and Functional Near-Infrared Spectroscopy," Front. Neurosci. **14**, 300 (2020).
24. R. Choe, T. Durduran, G. Yu, M. J. Nijland, B. Chance, A. G. Yodh, and N. Ramanujam, "Transabdominal near infrared oximetry of hypoxic stress in fetal sheep brain in utero," Proc. Natl. Acad. Sci. U.S.A. **100**(22), 12950–12954 (2003).
25. L. Wang, J. M. Cochran, T. Ko, W. B. Baker, K. Abramson, L. He, D. R. Busch, V. Kavuri, R. L. Linn, S. Parry, A. G. Yodh, and N. Schwartz, "Non-invasive monitoring of blood oxygenation in human placentas via concurrent diffuse optical spectroscopy and ultrasound imaging," Nat. Biomed. Eng **6**(9), 1017–1030 (2022).
26. D. Borycki, O. Kholiqov, S. P. Chong, and V. J. Srinivasan, "Interferometric Near-Infrared Spectroscopy (iNIRS) for determination of optical and dynamical properties of turbid media," Opt Express **24**(1), 329–354 (2016).
27. D. Borycki, O. Kholiqov, and V. J. Srinivasan, "Interferometric near-infrared spectroscopy directly quantifies optical field dynamics in turbid media," Optica **3**(12), 1471–1476 (2016).
28. O. Kholiqov, D. Borycki, and V. J. Srinivasan, "Interferometric near-infrared spectroscopy (iNIRS): performance tradeoffs and optimization," Opt. Express **25**(23), 28567–28588 (2017).
29. O. Kholiqov, W. J. Zhou, T. W. Zhang, V. N. Du Le, and V. J. Srinivasan, "Time-of-flight resolved light field fluctuations reveal deep human tissue physiology," Nat Commun **11**(1), 391 (2020).
30. L. Mei, G. Somesfalean, and S. Svanberg, "Frequency-modulated light scattering interferometry employed for optical properties and dynamics studies of turbid media," Biomed. Opt. Express **5**(8), 2810–2822 (2014).
31. J. M. Tualle, H. L. Nghiem, M. Cheikh, D. Ettori, E. Tinet, and S. Avrillier, "Time-resolved diffusing wave spectroscopy beyond 300 transport mean free paths," J. Opt. Soc. Am. A **23**(6), 1452–1457 (2006).
32. S.-J. Liu, S. Y. Lee, C. Pivetti, E. Kulubya, A. Wang, D. L. Farmer, S. Ghiasi, and W. Yang, "Transabdominal fetal signals measurement using fiber-based frequency-modulated continuous-wave near-infrared spectroscopy in a fetal lamb model," in *Biophotonics Congress: Optics in the Life Sciences 2023 (OMA, NTM, BODA, OMP, BRAIN)*(Optica Publishing Group, Vancouver, British Columbia, 2023), p. DW4A.6.
33. M. Rupawala, H. Dehghani, S. J. E. Lucas, P. Tino, and D. Cruse, "Shining a Light on Awareness: A Review of Functional Near-Infrared Spectroscopy for Prolonged Disorders of Consciousness," Front. Neurol. **9**, 1 (2018).

Biomedical Optics EXPRESS

34. L. Kocsis, P. Herman, and A. Eke, "The modified Beer-Lambert law revisited," Phys. Med. Biol. **51**(5), N91–8 (2006).
35. P. L. Carson, J. M. Rubin, and E. H. Chiang, "Fetal depth and ultrasound path lengths through overlying tissues," Ultrasound Med Biol **15**(7), 629–639 (1989).
36. Q. Fang and D. A. Boas, "Monte Carlo Simulation of Photon Migration in 3D Turbid Media Accelerated by Graphics Processing Units," Opt. Express **17**(22), 20178–20190 (2009).
37. D. Fong, A. Knoesen, and S. Ghiasi, "Transabdominal fetal pulse oximetry: The case of fetal signal optimization," in *2017 IEEE 19th International Conference on e-Health Networking, Applications and Services* (Healthcom), 1–6 (2017).
38. S. Ijichi, T. Kusaka, K. Isobe, K. Okubo, K. Kawada, M. Namba, H. Okada, T. Nishida, T. Imai, and S. Itoh, "Developmental changes of optical properties in neonates determined by near-infrared time-resolved spectroscopy," Pediatr. Res. **58**(3), 568–573 (2005).
39. A. B. Modena and S. Fieni, "Amniotic fluid dynamics," Acta Biomed **75**(Suppl 1), 11–13 (2004).
40. E. Zahedi and G. K. Beng, "Applicability of adaptive noise cancellation to fetal heart rate detection using photoplethysmography," Comput. Biol. Med. **38**(1), 31–41 (2008).
41. X. Zhou, Z. Chen, H. Chen, J. Li, and J. Hou, "Mode field adaptation between single-mode fiber and large mode area fiber by thermally expanded core technique," Opt. Laser Technol. **47**, 72–75 (2013).
42. X. Zhou, Z. Chen, H. Zhou, and J. Hou, "Mode-field adaptor between large-mode-area fiber and single-mode fiber based on fiber tapering and thermally expanded core technique," Appl. Opt. **53**(22), 5053–5057 (2014).
43. M. Veettikazhy, A. Kragh Hansen, D. Marti, S. Mark Jensen, A. Lykke Borre, E. Ravn Andresen, K. Dholakia, and P. Eskil Andersen, "BPM-Matlab: an open-source optical propagation simulation tool in MATLAB," Opt. Express **29**(8), 11819–11832 (2021).
44. J. U. Kim, Y. J. Lee, J. Lee, and J. Y. Kim, "Differences in the Properties of the Radial Artery between Cun, Guan, Chi, and Nearby Segments Using Ultrasonographic Imaging: A Pilot Study on Arterial Depth, Diameter, and Blood Flow," Evid Based Complement Alternat Med **2015**, 1 (2015).
45. A. Torricelli, D. Contini, A. Pifferi, M. Caffini, R. Re, L. Zucchelli, and L. Spinelli, "Time domain functional NIRS imaging for human brain mapping," NeuroImage **85**, 28–50 (2014).
46. P. Lanka, A. Segala, A. Farina, S. Konugolu Venkata Sekar, E. Nisoli, A. Valerio, P. Taroni, R. Cubeddu, and A. Pifferi, "Non-invasive investigation of adipose tissue by time domain diffuse optical spectroscopy," Biomed. Opt. Express **11**(5), 2779–2793 (2020).
47. S. Samaei, P. Sawosz, M. Kacprzak, Z. Pastuszak, D. Borycki, and A. Liebert, "Time-domain diffuse correlation spectroscopy (TD-DCS) for noninvasive, depth-dependent blood flow quantification in human tissue in vivo," Sci. Rep. **11**(1), 1817 (2021).